Since January 2020 Elsevier has created a COVID-19 resource centre with free information in English and Mandarin on the novel coronavirus COVID-19. The COVID-19 resource centre is hosted on Elsevier Connect, the company's public news and information website.

Bioelectrochemistry 145 (2022) 108096

Contents lists available at ScienceDirect

Bioelectrochemistry

journal homepage: www.journals.elsevier.com/bioelectrochemistry

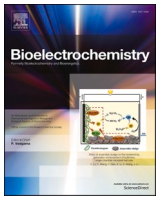

Design and simulation of a millifluidic device for differential detection of SARS-CoV-2 and H1N1 based on triboelectricity

Tara Ghafouri, Negin Manavizadeh *

Nanostructured-Electronic Devices Laboratory, Faculty of Electrical Engineering, K. N. Toosi University of Technology, Tehran 1631714191, Iran

ARTICLE INFO

Keywords:
Respiratory diseases
Virus detection
Antibody-antigen interaction
Electric double layer (EDL)
Triboelectric effect

ABSTRACT

Differential diagnosis of pathogenic diseases, presently coronavirus disease 2019 (COVID-19) and influenza, is crucial with due attention to their superspreading events, presumably long incubation period, particular complications, and treatments. In this paper, a label-free, self-powered, and ultrafast immunosensor device working based on triboelectric effect is proposed. Equilibrium constants of specific antibody-antigen reactions are accompanied by IEP-relevant electric charges of antigens to recognize SARS-CoV-2 and H1N1. Simulation attributes including fluid flow and geometrical parameters are optimized so that the maximum capture efficiency of 85.63% is achieved. Accordingly, antibody-antigen complexes form electric double layers (EDLs) across the channel interfaces. The resultant built-in electric field affects the following external electric field derived from triboelectricity, leading to the variation of open-circuit voltage as a sensing metric. The device is flexible to operate in conductor-to-dielectric single-electrode and contact-separation modes simultaneously. While the detection limit is reduced utilizing the single-electrode mode compared to the latter one, surface treatment of the triboelectric pair contributes to the sensitivity enhancement. A threshold value equal to −4.113 V is featured to discriminate these two viruses in a vast detectable region; however, further surface engineering can allow the on-site detection of any electrically-charged pathogen applying the emerging triboelectric immunosensor enjoying a lower detection limit.

1. Introduction

The ongoing outbreak of severe acute respiratory syndrome coronavirus 2 (SARS-CoV-2) Infection has augmented the significance of early-stage detection and management of patients with suspected coronavirus disease 2019 (COVID-19) to impede epidemics and pandemics. Detection techniques of viral agents are divided into cell culture, molecular approaches relevant to nucleic acid detection (*e.g.*, polymerase chain reaction (PCR) [1] and loop-mediated isothermal amplification (LAMP) [2]), serology based on antibody testing (*e.g.*, enzyme-linked immunosorbent assay (ELISA) [3] and rapid diagnostic tests such as lateral flow immunoassay (LFIA) [4]), direct imaging, and surface characterization [5]. Although molecular tests are mainly "gold standards" with the highest analytical sensitivity and specificity, most of them suffer from being resource-limited and complicated, lengthy technical procedures, and costly apparatus [6,7].

Aside from clinical detection methods, micro-total analysis systems (μ-TAS) such as point-of-care (PoC) devices emerged to achieve lab-on-a-chip technology; accordingly, antigen/antibody rapid detection tests have evolved the biosensor industry in virtue of low sample requirement, portable and high-throughput detection, easy-to-operate, cost- and time-effective monitoring of health conditions, and great accessibility on the user's end with comparable accuracy and sensitivity [8]. Early PoC diagnosis based on nucleic acid tests, immunoassays, and state-of-the-art biosensors is thus conducive to epidemic control and timely treatment [9–11]. Besides, to overcome misdiagnosis and low accuracy in PoC diagnostic devices, efforts have been made in line with developing sensitive detection methods based on high-performance transducers and amplifiers. A paper electrode-based pressure-tight sensor has been modified with multiwalled carbon nanotubes as a signal amplification for PoC immunoassay of carcinoembryonic antigen (CEA) with digital multimeter readout [12]. Analogously, an electrochromic device has been integrated with a pressure-based immunoassay to detect CEA using the capture antibody and Pt nanoparticles-labeled detection antibody in a reaction cell. In these sensing platforms, signal amplification is prompt due to the outstanding catalytic ability of Pt nanoparticles and the huge volume change from liquid (H_2O_2) to gas (O_2) [13]. Synergetic sensing effect of self-powered photoelectrochemical

* Corresponding author.
E-mail address: manavizadeh@kntu.ac.ir (N. Manavizadeh).

https://doi.org/10.1016/j.bioelechem.2022.108096
Received 17 December 2021; Received in revised form 9 March 2022; Accepted 13 March 2022
Available online 16 March 2022

immunoassay catalyzed with chemiluminescence-functionalized Au nanoparticles and a phosphomolybdic acid-based photochromic visualization platform has been revealed on rapid detection of disease-related protein [14]. Moreover, a self-powered photothermal – thermoelectric coupled immunoassay of α-fetoprotein exhibited a low detection limit over a wide linear range [15]. Subsequently, nanozyme-based [16], fluorescence resonance energy transfer (FRET)-based [17], optical [18], piezoelectric and magnetostrictive [19], surface acoustic wave [20], and electrochemical [21] immunosensors have been developed up to this point for the detection of viral respiratory infections. Among them, nanomaterial-based electrochemical sensors have grabbed attention owing to their ability to directly identify the analyte in low concentrations with increased sensitivity and reduced response time and signal noise [22]. In addition, electrochemical biosensors are the most consistent with the general trend toward acceleration and simplification of the bioanalytical process [57]. Recently, a molecularly imprinted polypyrrole (MIP)-based electrochemical sensor has been designed to detect SARS-CoV-2 spike glycoprotein. Pulsed amperometric detection was applied as an electroanalytical method [24]. In a label-free SARS-CoV-2 immunoglobulin G (IgG) sensor based on an organic electrochemical transistor, sensitivity has been enhanced by increasing Debye length and protein net charge through regulation of electrolyte ion concentration and pH value, respectively [25].

In this regard, microfluidics-based diagnostic systems facilitate the addressing and screening of infectious agents by integration of sample preparation, preprocessing, reaction, and detection steps into a miniaturized chip [26]; thus, microfluidic systems combined with PoC tests have excellent potential to accurately and conveniently quantify antigens/antibodies and biomarkers [27,28]. Microfluidic PoC equipment can meet the low-cost real-time detection within minutes [10]. Notably, the precise manipulation of molecular interactions allows for miniaturization and rapid processing of samples, with experimental techniques in lab-on-a-chip analytical platforms [29]. An electrochemical microfluidic immunosensor array has provided multiple measurement data for co-infection markers from a single run with remote capability [30]. The transduction of the target-induced molecular activation into an enhanced electrochemical signal has been attained by way of a system integrating reconfigurable responsive nanostructures and automated microfluidics [31] to detect SARS-CoV-2 specific RNA directly and enhance signaling catalytically.

To approach benchmark standardization of PoC devices, the world health organization (WHO) enacted a set of criteria for an ideal test in a health care system, so-called by the acronym *ASSURED* – Affordable, Sensitive, Specific, User-friendly, Robust and Rapid, Equipment-free, and Deliverable to remote areas [32]. Most of the aforementioned detection techniques, except for laboratory-based ones, are potent to meet the *ASSURED* criteria; however, the efficiency of electrochemical assays is further limited by the requirements of electrically powered, expensive equipment in developing nations. Therefore, integration of real-time connectivity, detection, and read-out steps into an automated, self-powered PoC device is desired. Recently, triboelectric nanogenerators (TENGs), developed initially for high-efficiency energy harvesting, are used as self-powered biosensors and PoC monitoring devices simultaneously [33,34]. In such cases, the interaction of a biological target with one of the triboelectric pairs (transducer) changes the triboelectric output adopted directly as a sensing signal.

At present, the differential diagnosis between respiratory tract infections, prominently influenza A and SARS-CoV-2, is critical in proper treatment and outbreak control. COVID-19 and influenza share many resemblances in transmission route and symptoms, inflicting misdiagnosis, cross-infection, treatment delay, and unnecessary wastage of medical resources [35]. This work demonstrates the detectability of these viruses based on the Ag-Ab binding affinity and isoelectric point (IEP)-relevant net charge of the receptor-binding domains (RBDs) on their surface proteins. The design of the proposed millifluidic TENG device is flexible to operate in both vertical contact-separation and single-electrode modes. Geometry- and fluid flow-related optimizations are performed to maximize the viral capture efficiency and triboelectric output signals concurrently. The triboelectricity-driven immunosensing extracted along with the open-circuit voltage (V_{oc}) and short-circuit charge transfer (Q_{sc}) contribute to detecting electrically charged viral agents in the electrolyte. Surface treatment is also applied to enhance the sensitivity and reduce the detection limit.

2. Detection platform and biosensing mechanism

The proposed immunosensing device combines a biological recognition mechanism (triboelectricity) with antibodies immobilized to the transducer, which generates a measurable signal in response to the presence of antigens in an infected analyte. Indeed, this device operates based on antigen-antibody interactions and identifies antigens attributed to the respiratory viruses with common symptoms and different medications, SARS-CoV-2 and H1N1, as model viruses of microorganisms (VoMs).

Since the protein is detected on the signal-transducing surface in biosensors, the development of such sensors necessitates the design of a surface with sufficient protein recognition capabilities [36]. Regarding TENG-based biosensors, surface engineering is a substantial element, especially in Ag-Ab affinity sensors [58]. Like the molecular assay, the antigen detection method allows defining the presence of a current viral infection, whereas the principle of the test procedure is similar to that of the serological assay and is based on the detection of specific antigen-antibody complexes. Definitely, appropriate treatment of the friction materials is needed to offer a selective TENG-based sensor. Here, antibodies immobilized on the bottom electrode capture the target antigens specifically and rectify this concern. Once virus-free and once again, virus-contained PBS electrolytes are injected into the millichannel continuously and contacted with the bottom electrode directly. The corresponding output voltages are compared to calculate and analyze the sensitivity and other performance criteria. The device structure consists of a millichannel made from an arbitrary biocompatible material, a Polydimethylsiloxane (PDMS) cap as an electron-acquiring triboelectric layer, an aluminum top electrode as an electron-donating triboelectric film above the PDMS layer, SARS-CoV-2 anti-spike IgG immobilized on the surface of Au bottom electrode through physical adsorption, and an electrolyte medium including antigen (SARS-CoV-2 spike protein (SCoV)) suspended in a PBS solution (pH 7.4). SARS-CoV-2 IgG is bound with spike protein through Ag-Ab reaction during incubation according to eq. (1):

$$IgG(ads) + SCoV \underset{k_d}{\overset{k_a}{\rightleftarrows}} IgGSCoVcomplex; inPBSsolution \tag{1}$$

Markedly, Antibody and antigen surface proteins comprised of zwitterionic amino acid sequences with positively- or negatively-charged functional groups corresponding to the IEP and pH values of the electrolyte. Most of the therapeutic monoclonal antibodies (mAbs) in infected human serum, *e.g.*, anti-SARS-CoV-2 IgG and anti-H1N1 IgG, suggest IEP values above 8.0 and thereby carry a slight net positive charge in phosphate-buffered saline (PBS) solution (pH 7.4) [25]. Moreover, each virion keeps its RBDs distribution, being consistent with specific cell receptors on the host cell's membrane [6]. The spike (S) protein of SARS-CoV-2 is composed of S1 and S2 subunits, mediating the receptor recognition and infection of SARS-CoV-2 [37]. It has been recently demonstrated that in the charged amino acids in RBDs of S1 and S2 units, positive and negative charges predominate, respectively [38]. This observation is compatible with their IEP ranges of 7.30 ~ 8.37 and 4.41 ~ 5.87, respectively, in the electrolyte pH 7.4 [39]. Furthermore, the seasonal influenza A virus can be divided into subtypes based on the glycoproteins (hemagglutinin and neuraminidase) present in the viral envelope. Under the physiological condition (neutral pH level), both RBD proteins of H1N1 have an IEP range of 4.25 ~ 4.50, deduced

negatively charged [40]. The charged molecules, therefore, throw their impact on the surface potential of the electrodes in a transducer converting biological signals into electrical ones. The main idea is that the electric charges of antigenic protein and the subsequent Ag-Ab complex induce an electric dipole due to inhomogeneity and, as a result, an immunoelectrophoresis field during the triboelectrification. These dipoles undergo potential drops across the two electric double layers (EDLs) on the PDMS/electrolyte and the bottom electrode/electrolyte interfaces. Consequently, the charged complexes on the bottom electrode can change the surface potential leading to a shift of the open-circuit voltage arising from the triboelectric effect.

In addition, to develop a sensitive immunosensor for virus detection, the physicochemical information of the kinetics of specific antibodies and nucleoprotein binding is predominant. Association and dissociation rate constants (k_a and k_d) are representatives of the strength of Ag-Ab or receptor-ligand affinity interaction. The strength is a result of a set of intermolecular forces involving Van der Waals forces, hydrogen or ion-dipole bonds, hydrophobic, and electrostatic interactions between oppositely-charged antigen and antibody protein structures [41]. Therefore, the equilibrium constants imply an electrical nature accompanied by RBD electric charge. Long-range forces such as electrostatic and hydrogen bonds are important in the rate of formation of antigen-antibody complexes at the points of contact (*i.e.*, binding affinity); while the short-range forces contribute significantly to bond strength by reducing the rate of complex dissociation. Interaction kinetics of SARS-CoV-2 nucleoproteins and specific antibodies against these proteins have been determined through total internal reflection ellipsometry [42]. Applying this technique, high sensitivity of spectroscopic ellipsometry is achieved in combination with the surface plasmon resonance effect [43].

3. Device flexibility in operation modes

TENGs operate based on the coupling of contact electrification and subsequent electrostatic induction. When two materials of typically significant discrepancies in their charge donation/acquisition properties (*e.g.*, polarity and dielectric constant) are brought into contact with or rubbed against each other, the charge neutrality disappears, and two surfaces acquire equivalent but opposite charges. Electrostatic charges induced on the back-electrodes further generate a potential drop, driving electrons to flow between the two electrodes [25]. Taking four operation modes of TENG into account, lateral sliding and freestanding modes require an additional surface modification such as super-hydrophobicity for fluid-based TENGs [44]. It is arising from the fact that the higher the surface hydrophobicity, the larger the effective contact area with the analyte; subsequently, the superior the triboelectric outputs. Hence, vertical contact-separation and single-electrode modes mainly simplify the structural design; especially, fluid-based TENGs enjoy a relatively stable output and durability [45].

3.1. Dielectric-to-conductor contact-separation mode

Assuming the triboelectric pair (PDMS and Al top electrode as a counter triboelectric material) is fully-contacted, the electroneutrality is preserved. Upon separating (releasing step), equal and, opposite surface charges are generated on the electrodes. During electrification, the Al electrode loses electrons and becomes positively charged; while, PDMS gains electrons and becomes negatively charged. The resultant electric potential during the separation process drives the migration of electrons from the bottom electrode to the top one through a circuit to balance the change in the electric potential caused by the electrostatic induction. Further, approaching the triboelectric elements in the pushing step results in electrons flowing in the opposite direction, and a change in the polarity of the electric potential is attained. The procedure is represented schematically in Scheme 1. Since the electrolyte and the bottom electrode are in contact, potential distribution on the Au electrode can induce the electrical reaction between them. Indeed, the electrolyte contributes also to the balancing process in virtue of the present electric potential.

3.2. Dielectric-to-conductor single-electrode mode

In this configuration, electrostatic neutrality can be achieved by electron transfer between the bottom electrode, the reference electrode connected with the ground, and the electrolyte. The resultant potential difference is regarded thereby as a sensing metric. Like the contact-separation mode, the potential distribution leads to the charge transfer from the ground to the bottom electrode, and inverse, generating the electric current (Scheme 2). As demonstrated further, although output signal levels are more pronounced in contact-separation mode, the single-electrode mode allows reflecting the presence of the antigenic targets more strongly. It is attributed to the fact that the transferred electrons onto the top electrode could be conserved with due attention to the lack of direct electrical connection between the top and bottom electrodes.

4. Simulation strategy and numerical modeling

The proof-of-concept simulations have been accomplished in COMSOL Multiphysics 5.6 software applying the finite-element method to discretize the equations. The antigenic analyte is flown from the lower inlet. At the same time, the buffer solution is injected through the upper one with a velocity field ratio of 0.166 mm/s to 0.238 mm/s, respectively, proportional to the whole device length and the required

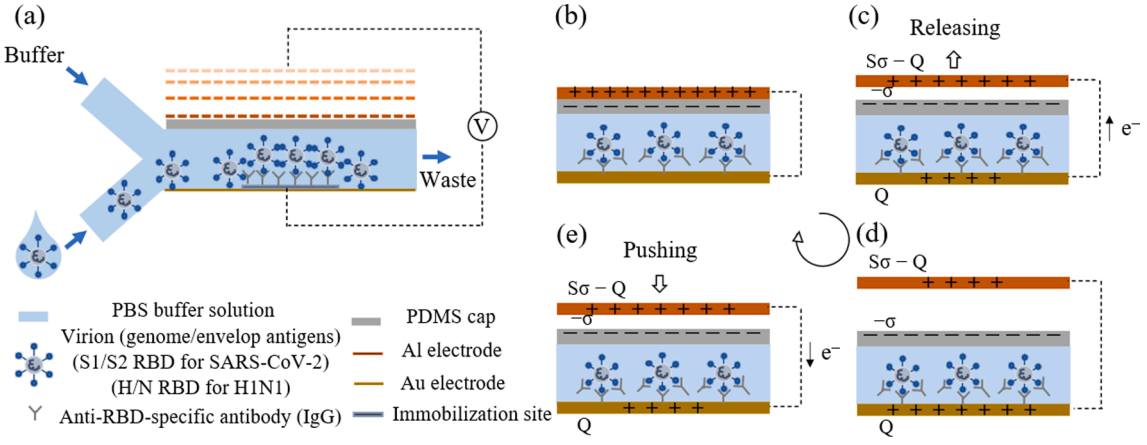

Scheme 1. (a) Illustration of the proposed TENG immunosensor and (b-e) the working procedure based on contact-separation mode.

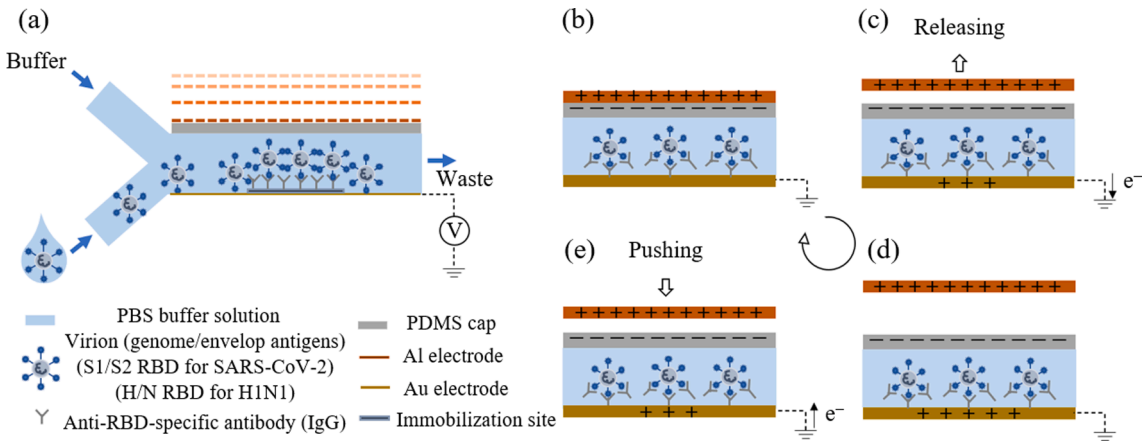

Scheme 2. (a) Illustration of the proposed TENG immunosensor and (b-e) the working procedure based on single-electrode mode.

incubation period. This configuration will squeeze viral antigens from the lower inlet close to the mAb-immobilized bottom electrode region. According to Eq. (1), Ag-Ab interaction kinetics with two equilibrium reactions are defined in a 0D reaction column to direct specific background bindings on the bottom electrode surface. This procedure is implemented through a Reaction Engineering interface coupled further to a 2D model including Chemistry, Transport of Diluted Species, Surface Reactions, Laminar Flow, and Electrostatics modules. To model the behavior of an analyte based on triboelectric effect, coupling of two physics interfaces of Electrostatics and Transport of Diluted Species is required in the form of Nernst-Planck-Poisson equation:

$$\begin{cases} J_i = -D_i\nabla c_i - u_{m,i}z_iFc_i\nabla V \\ \nabla.(-\varepsilon\nabla V) = \rho \end{cases} \rightarrow \frac{\partial c_i}{\partial t} + u_i\nabla c_i - \nabla.\left[D_i\left(\nabla c_i + \frac{z_iec_i}{k_BT}\nabla V\right)\right] = 0 \rightarrow -\nabla.(\varepsilon\nabla V) = \sum_i z_iec_i \tag{2}$$

desired velocity from both inlets. Figures S2 and S3 illustrate concentrations of the Ag solution applied into the millichannel and the corresponding Ag-Ab complex produced, respectively, during which time interval the solution passes through the device. In the following, the abovementioned attributes are optimized to maximize the viral capture efficiency.

4.1. Viral capture efficiency

Since viral capture efficiency is correlated further with the voltage shift of the bottom electrode, we investigate the factors affecting this figure-of-merit at the first step, which is defined as:

$$Viralcaptureefficiency_{Max.}[\%] = \frac{ConcentrationofAg - Abcomplexonimmobilizationsite}{InputAgconcentration} \times 100 \tag{3}$$

The Nernst-Planck equation represents the electrodiffusion (J_i) of the charged species in terms of their concentration (c_i) in an electrolyte. In this equation, D_i, u_i, z_i, F, k_B, T, V, ε, and ρ denote diffusion coefficient, mass averaged velocity, charge quantity, Faraday's constant, Boltzmann constant, absolute temperature, electric potential, dielectric constant, and charge density. The first term in the definition of J_i is the flux due to diffusion, and the second one interprets the flux due to electromigration. The Poisson equation describes the electrostatic interaction of the charged nanoparticles immersed in an electrolyte and the subsequent formation of EDL, leading to electrokinetic phenomena ($E = -\nabla V$). The terms ε, ρ, and E denote permittivity (mainly for the solvent), free charge density, and electric field, respectively [46].

The millifluidic channel has a length of 5 cm, a width of 1 cm, and a height of 1 mm as the default. The viral antigen concentration varies in a range of $10^4 \sim 10^9$ particles/ml. Accordingly, the concentration ratio of the antigenic solution to the viral-free buffer solution is considered in the range of $10^{-16} \sim 10^{-11}$ throughout the simulation. The molar mass of serum-specific IgG equals 700 ~ 1600 mg/dl, and its molecular weight is 150 ~ 170 kDa; therefore, IgG concentration is assumed 46 ~ 106 μmol/m^2. In addition, the viral flow rate and the reactive patch size (mAb immobilization site) are regarded as 0.1 ml/min and 3 cm, respectively, as the default. Figure S1 indicates the velocity magnitude and pressure contour of the streaming flow, which enables fluid flow at

The capture efficiency is a function of the viral Ag to immobilized mAb concentration ratio, the flow rate of Ag solution, reactive patch size, the equilibrium constant in the Ag-Ab binding, and diffusion coefficients of Ag and Ab. Fig. 1(a) illustrates the increment of Ag-Ab concentration proportional to the accessible Ag concentration. This rise continues until the increased Ag concentration is comparable to mAb concentration, leading to an efficiency drop, as shown in Fig. 1(b). Similarly, increasing the mAb concentration to a certain extent, depending on the Ag concentration, contributes to enhancing the produced species [Fig. 1(c) and (d)]. On the other hand, the test time for such a label-free device is mainly limited by the incubation period of antigens on the sensor; hence, the flow rate of the Ag solution is another influential component that can affect the incubation time. The large velocity fields impede the appropriate Ag-Ab binding, and it is failed to produce an adequate specific Ag-Ab complex for the detection of target species [Fig. 1(e)]. Moreover, the broader the mAb immobilization area is devised, the higher the binding capacity is provided, and the higher efficiency is achieved, as shown in Fig. 1(f).

Apart from the distinction of virus particles in terms of their IEP-relevant RBD net charge, the association and dissociation rate constants of the corresponding specific Ag-Ab can be also distinct for different viruses. The strength of the Ag-Ab interaction is measured by the affinity constant, which is defined according to:

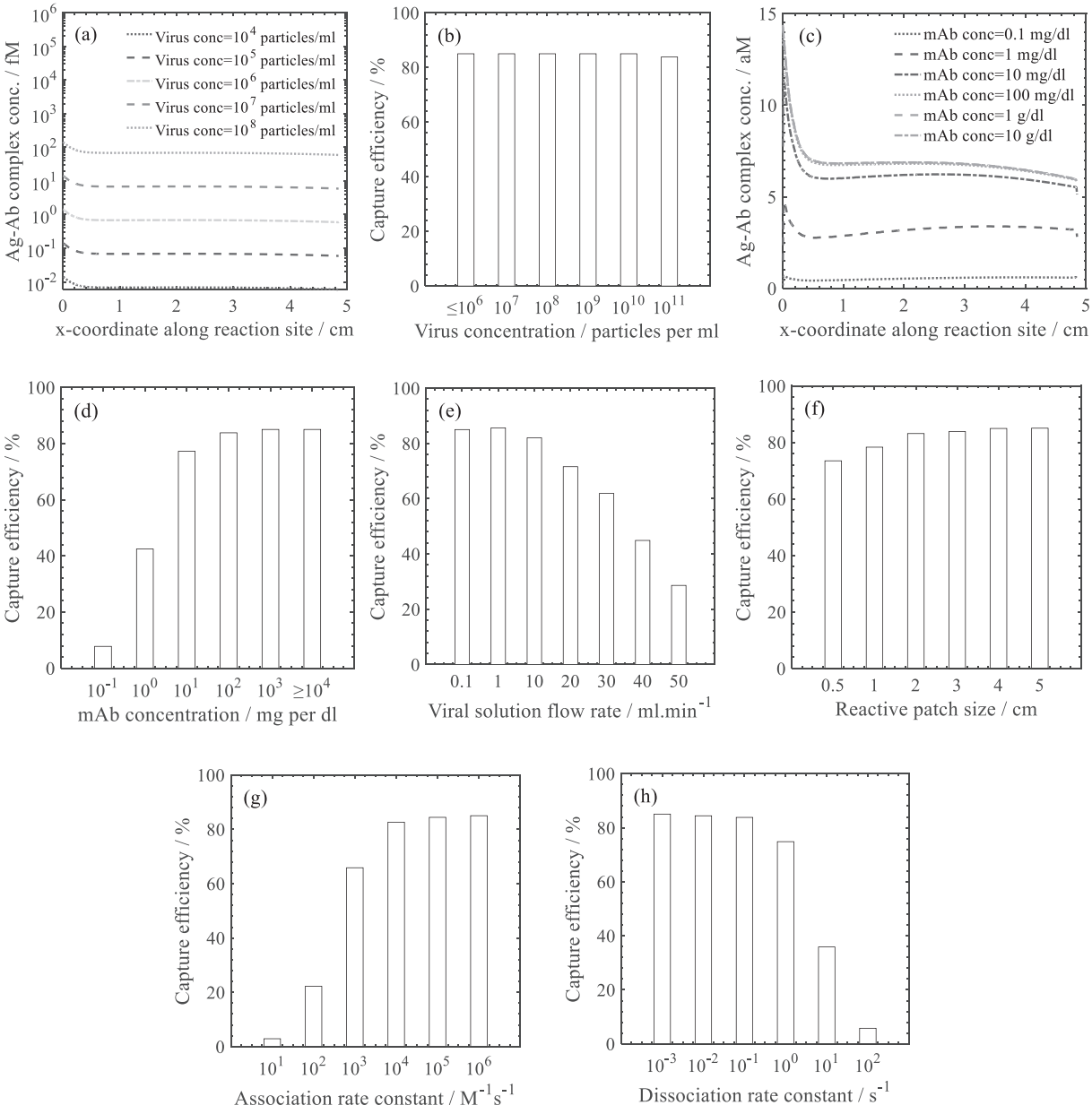

Fig. 1. Dependency of the antigen-antibody product concentration and capture efficiency on (a,b) antigen concentration injected into the channel, (c,d) antibody concentration immobilized on the transducer surface, (e) antigenic solution velocity field, (f) immobilization site, (g) forward rate constant, and (h) reverse rate constant in Eq. (1).

$$k_A = \frac{[Ag - Ab]}{[Ag][Ab]} \tag{4}$$

where [Ag] and [Ab] denote molar concentrations of unoccupied binding sites on the antigen and antibody, respectively, and [Ag-Ab] represents the molar concentration of the antigen-antibody complex in the bulk solution. Indeed, the affinity constant describes how many Ag-Ab complexes per volume are formed at the moment equilibrium is reached [47]. The time required for this to occur depends on diffusion coefficients of Ag and Ab. Also, the immunocomplex concentration adjacent to the immobilization surface ($[Ag - Ab]_s$) can be expressed by the Boltzmann distribution [48]:

$$[Ag - Ab]_s = [Ag - Ab]\exp(-e\psi_s/k_BT); \tag{5}$$

in which ψ_s denotes the surface potential. Therefore, the affinity constant can in turn modulate the triboelectric output voltage, as seen further. These considerations and the relevant parameters have been applied throughout simulations to distinct SARS-CoV-2 and H1N1 antigens. Fig. 1(g) and (h) represent that the larger the association rate and/or the smaller the dissociation rate, the higher the capture efficiency. The kinetic parameters (k_a and k_d) used here have been calculated with a surface plasmon resonance imaging (SPRi) platform, corresponding to a virtual ligand-based screening that targets pockets on each side of binding sites on the RBD. Selected protein-grafted regions in the SPR images were analyzed, and the average reflectivity variations of the chosen areas were yielded as a function of time. Real-time binding signals were recorded and analyzed by Data Analysis Module [49]. The affinity parameters of recombinant SARS-CoV-2 (spike) and H1N1 (hemagglutinin) RBD proteins are consistent with those of related studies [42,50]. Considering these quantities according to Table 1, the highest capture efficiency equal to 85.63% is attained for the proposed immunosensor device.

Table 1
Physiochemical and geometrical parameters for simulation of the TENG immunosensor device in COMSOL.

Category	Quantity	Value
Fluid flow	Antigen (spike protein) molar mass [kDa]	76.5
	Antibody (anti-spike protein IgG) molar mass [kDa]	150
	Antigen concentration [mol/m^3]	1.66×10^{-12}
	Antibody concentration [mol/m^2]	3.80×10^{-5}
	PBS buffer concentration [mol/m^3]	151.50
	Antigenic solution flow rate [ml per min]	1
	PBS buffer flow rate [ml per min]	1.32
SARS-CoV-2 (Wild-type) Ag-mAb equilibrium reaction [38]	Diffusion coefficient for anion/cation in PBS [μm^2/s]	50 / 50
	Diffusion coefficient for Ag/mAb in PBS [cm^2/s]	8.62×10^{-8} / 2.81×10^{-7}
	pH of aqueous-phase mock medium in the channel	7.4
	Forward rate constant (k_a) [m^3 s^{-1} mol^{-1}]	175
	Reverse rate constant (k_d) [s^{-1}]	7.75×10^{-3}
Triboelectricity	Surface tribo-charge density of PDMS (σ) [nC/m^2]	−21.79
	Relative permittivity of PDMS layer	2.75
	Relative permittivity of electrodes	Infinite
	Relative permittivity of aqueous-phase mock medium	80
Device geometry	Reactive patch size on the bottom electrode [cm]	4.85
	Channel length [cm]	5
	Channel height [mm]	1
	PDMS layer thickness [mm]	0.50
	Thickness of electrodes [μm]	100
	Maximum separation distance [cm]	5

4.2. Triboelecricity-derived optimization of geometry

Posterior to the binding of the antigenic RBD of the spike protein with the anti-spike protein antibody specifically, the Al electrode is separated from the PDMS layer to drive triboelectricity in vertical contact-separation mode. The device dimensions are optimized so that enhanced output signals are achieved. A general equation that describes the charge-voltage relation in terms of separation distance (y) in triboelectric devices is given by:

$$V = -\frac{1}{C(y)} \times Q + V_{oc}(y) \tag{6}$$

Notably, in the open-circuit condition ($Q = 0$), the above equation is equivalent to $V = V_{oc}$, and in short-circuit condition ($V = 0$), we have $Q = Q_{sc} = C \times V_{oc}$, in which C denotes the capacitance between two electrodes. The V-Q-y relation is illustrated in Fig. 2(a) for the triboelectric millichannel with an Ag-contained mock medium. In virtue of electrostatic induction, the higher potential for counter electrode drives electron migration from the bottom electrode to the top one, as shown in Fig. 2(b). The minor asymmetry seen in the potential of Al and Au electrodes, particularly at higher distances, is attributed to the potential drop across EDLs in the electrolyte, according to Scheme 3. This difference reflects the presence of antigenic charged molecules (like SARS-CoV-2 Spike S2 RBD) near the antibody-immobilized bottom electrode and the subsequent formation of electric dipoles on its surface. In addition, Ag residues (like SARS-CoV-2 Spike S1 RBD) adjacent to the PDMS layer as well as cationic species of the PBS electrolyte can form an additional EDL at the PDMS/electrolyte interface leading to the electrophoresis. This implication can affect the electric field generated by tribo-charges transferred onto this layer and change in turn, the output signal (Figure S4). The result is a reduction in V_{oc} values, and a rise in Ag concentration intensifies V_{oc} drop explicitly, as depicted in Fig. 2(c). Apparently, EDL thickness in the electrolyte and PDMS layer affects the output signal level, which is in good agreement with [51]. Lengthening the channel in conjunction with enlarging the effective surface area of the triboelectric pair will mainly enhance the capacitance and subsequent charge transfer efficiency [Fig. 2(d)]. On the contrary, the channel height is inversely proportional to electric field strength and the resultant potential difference between electrodes [Fig. 2(e)]. Similarly, PDMS layer thickness will affect the potential distribution at the PDMS/electrolyte interface; thus, its increment weakens the output signal slightly [Fig. 2(f)]. According to Poisson's equation, the surface charge density, related to the dielectric, triboelectric materials applied in the device, is directly proportional to the potential gradient [Fig. 2(g)]. As a consequence, the geometrical parameters are opted according to Table 1 for further biosensing simulations so that the highest output magnitudes of V_{oc} and Qsc are provided.

5. Biosensing results and discussion

The detection process of the charged antigenic species involves the following two steps: (i) incubating an antigenic solution on the mAb-immobilized Au electrode for optimal 60 s; and (ii) applying an immunoelectrophoresis field stemming from the triboelectric effect. The underlying concept is the triboelectric response of the charged Ag-Ab complexes with different binding affinities in the PBS electrolyte under the physiological condition. An EDL is formed in the presence of the positively-charged anti-S protein mAb of SARS-Cov-2 and the negatively-charged antigen (S protein S1 RBD). The resultant electric field inflicts a potential upon the bottom electrode, which will further change the triboelectricity-driven electric field to balance the charge neutrality. The charge regulation is, therefore, eventuated considering interactions between unequally charged surfaces. Subsequently, an additional capacitance will ensue, affecting the output signal. The effective capacitance density (C_i) of the millifluidic channel is equal to the total capacitance of two capacitors in EDLs' interfaces ($C_{EDL_{(Up)}}$ and $C_{EDL_{(Down)}}$) connected in series according to:

$$C_i = \frac{C_{EDL_{(Up)}} C_{EDL_{(Down)}}}{\left(C_{EDL_{(Up)}} + C_{EDL_{(Down)}}\right) S} \tag{7}$$

in which S denotes active surface area. In this way, the geometry effect of the capacitance structure is excluded. The formation of dipoles on the Au electrode induces a shift in the potential of both electrodes in the same direction with different magnitudes (Scheme 3). As indicated in Fig. 3(a), the bottom electrode exposed to these dipoles is more susceptible as Ag concentration rises. According to Eq. (7), this potential difference is ascribed to the effective dielectric constant ($C = \Delta Q/\Delta V = \varepsilon_0 \varepsilon_r A/d$), being unique for each virus due to its protein/nucleic acid composition [52]. Fig. 3(b) shows that the presence of polar and/or charged Ag molecules in the PBS electrolyte generates an electric field weakening the triboelectricity-derived electric field around both electrodes, in conjunction with a minor additional charge transfer. Fig. 2(b) and 3(b) describe properly the charge regulation due to interaction forces between surfaces and modifications of the surface charge upon variations of the separation distance. This observation confirms the potential drop across EDLs in Scheme 3; in effect, the output signal will drop. Hence, the sensitivity is defined as the following for SARS-CoV-2 detection:

$$Response = \left| \frac{V_{oc_{(Antigen-freePBSmedium)}}}{V_{oc_{(Antigen-containedPBSmedium)}}} \right| \tag{8}$$

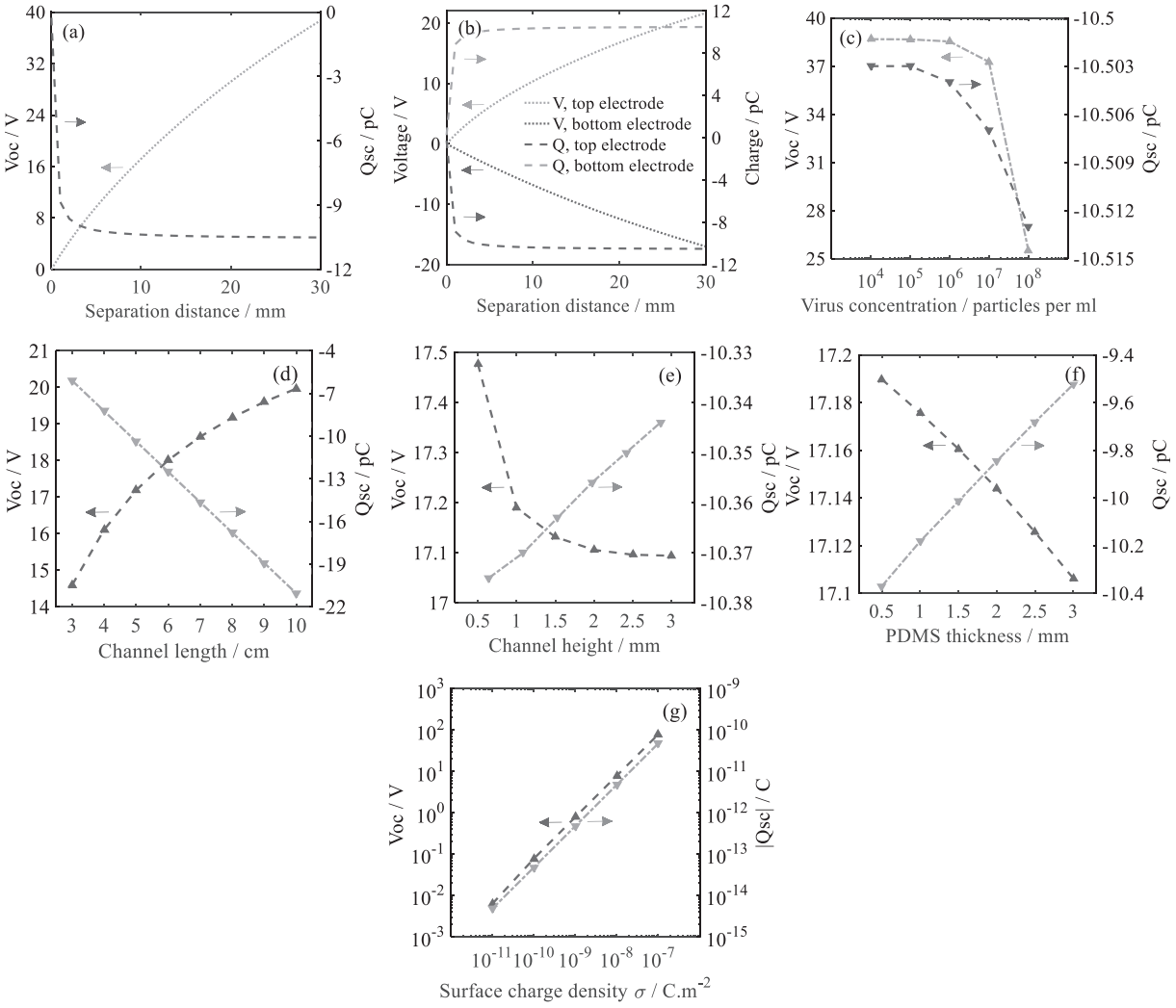

Fig. 2. Dependency of the output characteristics of the TENG immunosensor device on (a,b) separation distance, (c) viral antigen concentration, (d) channel length and (e) height, (f) thickness and (g) surface tribo-charge density of the triboelectric material.

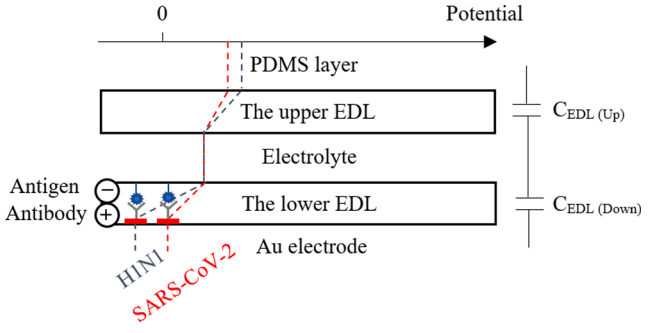

Scheme 3. Illustration of the dipole formation and potential drops in both EDLs through electrophoresis, which contributes further to the detection of viruses using the TENG immunosensor device.

Despite acquiring high sensitivity at high viral concentrations applying contact-separation mode, the detection limit is undesirable (≈ 10^6 particles per ml). Considering the single-electrode configuration, the output value of $|V_{oc}|$ is much lower than that of the contact-separation mode, as shown in Fig. 4(a). This can be ascribed to that the farther the top electrode is located, the poorer the effect on the electric field distribution around the electrodes is yielded (Figure S5); thus, the more limited the output is obtained. As a result, Q_{SC} plateaus slowly in single-electrode TENGs [Fig. 4(b)], in good consistency with [53]. However, the single-electrode mode is preferred for our sensing application with due attention to the two points: (i) this operation mode provides more resolution to selectively detect viral agents, especially in lower Ag concentrations in which V_{oc} values are relatively small and close for different antigenic biomolecules of viruses. This structure can be thus conducive to enhancing selectivity and lowering detection limit according to Fig. 4(a); (ii) the on-site detection only based on antigenic molecules bound to immobilized mAb is desired irrespective of any anionic/cationic species in the PBS electrolyte. The single-electrode structure realizes this purpose by fading the upper EDL effect. It is the reason why signal-ratio is almost unchanged for different separation distances, prior and posterior to the sensing, as represented in Fig. 4(b). To compensate for the deficiency of the sensitivity, the PDMS layer is patterned so that the influence of ions and counterions present in the PBS medium on the potential of the Au electrode is disappeared [Fig. 4 (c)]. Certainly, the stronger electric field through the edges in the semi-dome-shaped PDMS layer draws undesirable ionic species off (Figure S6).

As aforementioned in Section II, the difference in IEP values for antigenic proteins in SARS-CoV-2 and H1N1 in the same aqueous medium results in different immunoelectrophoresis fields across the lower EDL, inducing different potential distribution around the bottom electrode and the resultant sensing signal. The higher the antigen

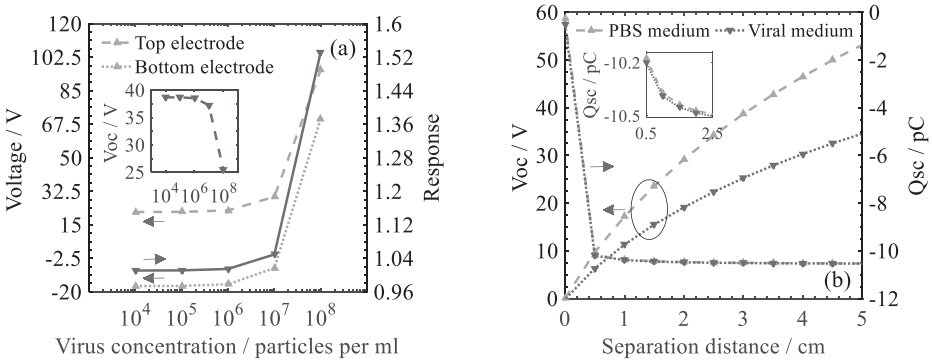

Fig. 3. SARS-CoV-2 sensing signal in terms of (a) viral antigen concentration in the PBS electrolyte and (b) separation distance in contact-separation mode.

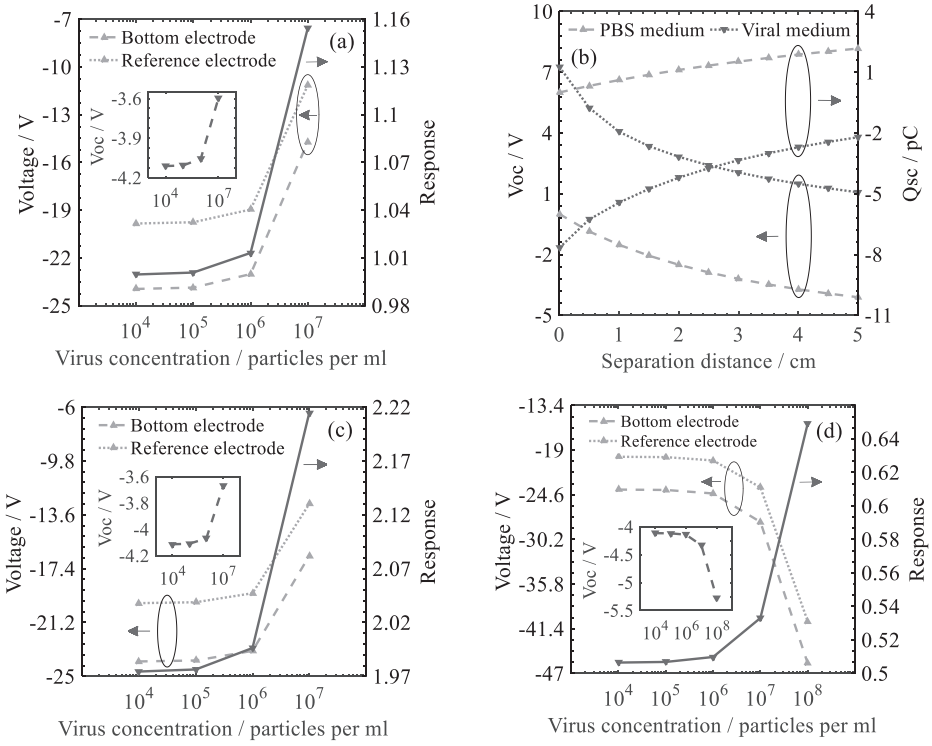

Fig. 4. SARS-CoV-2 sensing signal in terms of (a) viral antigen concentration in the PBS electrolyte and (b) separation distance in single-electrode mode applying planar and (c) semi-dome-shaped PDMS layers in the device structure; (d) the counterpart diagram presented in (c) for H1N1 detection.

concentration, the stronger the electrophoresis force. Cooperatively, different binding affinities (k_a and k_d) in specific Ag-Ab interactions for SARS-CoV-2 and H1N1 [54,55] augments the sensitivity by producing different concentrations of Ag-Ab complex for the same input viral concentration. By applying the optimal structure for the triboelectric immunosensor in the single-electrode mode, the sensitivity and detection limit of H1N1 sensing are studied and compared to those of SARS-CoV-2. Since both antigenic subunits in H1N1 are negatively-charged in PBS electrolyte (pH 7.4), the surface energy of the Au electrode can increase during triboelectrification. As a result, the potential magnitude increases with Ag concentration, unlike SARS-CoV-2, as indicated in Fig. 4(d). Accordingly, the numerator and denominator are substituted in Eq. (8) to maintain the concentration-response relation. As a distinguishing criterion, the landmark is −4.113 V so that sensing signals (V_{oc}) exceeding this value reveal the presence of SARS-CoV-2, taking the detection limit into account. While, for V_{oc} values inferior to this value, the H1N1 virus is identified. Furthermore, the detection limit represents a reduction of one order of magnitude for H1N1 detection compared to SARS-CoV-2.

Most of the electrochemical immunosensors developed to date are powered by batteries with the disadvantages of large-size, heavy-weight, frequent charging, and limited lifetime, hindering the modern designed conception of mobility and sustainability. Particularly, the probable heating and toxicity can lead to the infected cell lysis and low accuracy of the detection. Thus, a reliable and biocompatible power resource supplying the portable PoC sensor with no battery requirement has been suggested in this work. The proposed TENG-based device has been demonstrated to establish a platform for developing self-powered sensor systems and flexible electronics to harvest mechanical energy from the surrounding environment into electricity. Furthermore, the TENG-driven energy-autonomous sensor can be applicable everywhere and at any time with simple operation and fabrication. The device has the potential to meet the *ASSURED* criteria outlined by WHO for a successful low-cost diagnostic tool. On the other hand, a conventional method to flow zwitterionic and/or polarized particles in a suspension is dielectrophoresis, where high external DC/AC voltages are applied. The proposed triboelectric sensor has also suggested an appropriate solution to this issue with the least power consumption. In addition, the

biosensor can directly detect the viral agents without the use of tags, and thus, is known as a label-free assay. The rapid response is attributed to that the response time is constrained mainly to the incubation period of the specific Ag-Ab interaction and the required number of contact-separation cycles to attain stability in experiments, which is expected to be within minutes.

The proposed methodology adopted from electrical signatures of the associated viruses can be upgraded to be applied *in situ*, which will not only pave the way for direct and rapid detection of viruses in biological samples but also enable their early-stage detection in infected individuals. In comparison with the previous similar researches [25,52,56], it is expected that our proof-of-principle work will enjoy comparable performance metrics such as specificity and power consumption, and may in fact be superior in real samples.

6. Conclusion

In this paper, a label-free, self-powered, ultrafast, and simple millifluidic immunosensor was proposed to recognize SARS-CoV-2 and H1N1 infections based on the electrokinetic behavior of viral antigen-antibody complexes in conjunction with the implication of triboelectricity-driven electric field. The viral nucleic acid genomes are wrapped in proteins with zwitterionic amino acids; therefore, the net charge of a virus depends upon the cumulative charges of the genetic material and the protein. The main reason for choosing two similar viruses with almost the same symptoms and different medications was to demonstrate the sensitivity of the current method. The leading interaction of a virus particle with its surrounding medium occurs through antigenic proteins on its surface RBDs. In the best case, this binding eventuated an efficiency of 85.63% for SARS-CoV-2. Simulation results revealed that the resultant Ag-Ab detection species are directed with the generated immunoelectrophoresis field. Thence, the charge segregation derived from the presence of dipoles in the EDL induces an electrical potential profile across the interface, which affects the subsequent triboelectric open-circuit voltage. Meanwhile, to reach the optimal sensitivity and detection limit, distance dependency of the triboelectric outcomes was studied, taking contact-separation and single-electrode operation modes into account. As expected, irrespective of the type of the analyte applied, separation increment strengthens *Voc* and *Qsc* outputs. Nevertheless, the single-electrode configuration outperformed by eliminating the intervention of ionic species present in the electrolyte. Therefore, the detection limit decreased by about two orders of magnitude. In addition, surface engineering of the triboelectric pair led to an about 2x enhancement in the sensitivity. Significantly, the detection time is limited by the incubation period of antigens on the antibody-immobilized electrode as a signal transducer, less than a few minutes. The proposed triboelectric device as a self-powered active immunosensor can be a promising candidate for high-throughput and multiplexed detection of electrically charged pathogens with different IEPs and equilibrium constants of the corresponding antigen-antibody reaction in the same electrolyte.

Declaration of Competing Interest

The authors declare that they have no known competing financial interests or personal relationships that could have appeared to influence the work reported in this paper.

Appendix A. Supplementary material

Supplementary data to this article can be found online at https://doi.org/10.1016/j.bioelechem.2022.108096.

References

[1] M. Favaro, W. Mattina, E.S. Pistoia, R. Gaziano, P. Di Francesco, S. Middleton, S. D'Angelo, T. Altarozzi, and C. Fontana, "A new qualitative RT-PCR assay detecting SARS-CoV-2," *Sci, Rep.*, vol. 11, no. 18955, Sep. 2021.

[2] W.E. Huang, B. Lim, C.-C. Hsu, D. Xiong, W. Wu, Y. Yu, H. Jia, Y. Wang, Y. Zeng, M. Ji, H. Chang, X. Zhang, H. Wang, Z. Cui, RT-LAMP for rapid diagnosis of coronavirus SARS-CoV-2, Microbial. Biotech. 13 (4) (2020) 950–961.

[3] M.A. MacMullan, A. Ibrayeva, K. Trettner, L. Deming, S. Das, F. Tran, J.R. Moreno, J.G. Casian, P. Chellamuthu, J. Kraft, K. Kozak, F.E. Turner, V.I. Slepnev, L.M. L. Page, ELISA detection of SARS-CoV-2 antibodies in saliva, Sci. Rep. 10 (20818) (Nov. 2020) 1–8.

[4] D. Wang, et al., Rapid lateral flow immunoassay for the fluorescence detection of SARS-CoV-2 RNA, Nat. Biomed. Eng. 4 (Dec. 2020) 1150–1158.

[5] B.A.S. Machado, K.V.S. Hode, V.G. Barbosa-Júnior, M.B.P. Soares, R. Badaró, The main molecular and serological methods for diagnosing COVID-19: An overview based on the literature, Viruses 13 (40) (Dec. 2020) 1–36.

[6] G. Jenkins, C.D. Mansfield, Microfluidic diagnostics: Methods and protocols, 1st Edition, Humana press, Clifton, New Jersey, United States, 2013.

[7] J. Dronina, U. Samukaite-Bubniene, A. Ramanavicius, Advances and insights in the diagnosis of viral infections, J. Nanobiotechnol. 19 (348) (Oct. 2021) 1–23.

[8] M. Yang, Y. Tang, L. Qi, S. Zhang, Y. Liu, B. Lu, J. Yu, K. Zhu, B. Li, Y. Du, SARS-CoV-2 point-of-care (POC) diagnosis based on commercial pregnancy test strips and a palm-size microfluidic device, Anal. Chem. 93 (35) (Sep. 2021) 11956–11964.

[9] Q. Song, X. Sun, Z. Dai, Y. Gao, X. Gong, B. Zhou, J. Wu, W. Wen, Point-of-care testing detection methods for COVID-19, Lab Chip 21 (Feb. 2021) 1634–1660.

[10] S.-M. Yang, S. Lv, W. Zhang, Y. Cui, Microfluidic point-of-care (POC) devices in early diagnosis: a review of opportunities and challenges, Sensors 22 (4) (Feb. 2022) 1620.

[11] S. Jain, M. Nehra, R. Kumar, N. Dilbaghi, T.Y. Hu, S. Kumar, A. Kaushik, and C.-Z. Li, "Internet of medical things (IoMT)-integrated biosensors for point-of-care testing of infectious diseases," *Biosens. Bioelectron.*, vol. 179, p. 113074, May. 2021.

[12] Z. Yu, Y. Tang, G. Cai, R. Ren, D. Tang, Paper electrode-based flexible pressure sensor for point-of-care immunoassay with digital multimeter, Anal. Chem. 91 (2) (Dec. 2018) 1222–1226.

[13] Z. Yu, G. Cai, X. Liu, D. Tang, Pressure-based biosensor integrated with a flexible pressure sensor and an electrochromic device for visual detection, Anal. Chem. 93 (5) (Jan. 2021) 2916–2925.

[14] Z. Yu, H. Gong, Y. Li, J. Xu, J. Zhang, Y. Zeng, X. Liu, D. Tang, Chemiluminescence-derived self-powered photoelectrochemical immunoassay for detecting a low-abundance disease-related protein, Anal. Chem. 93 (39) (Sep. 2021) 13389–13397.

[15] L. Huang, J. Chen, Z. Yu, D. Tang, Self-powered temperature sensor with Seebeck effect transduction for photothermal–thermoelectric coupled immunoassay, Anal. Chem. 92 (3) (Jan. 2020) 2809–2814.

[16] V.S. Javalkote, N. Kancharla, B. Bhadra, M. Shukla, B. Soni, A. Sapre, M. Goodin, A. Bandyopadhyay, S. Dasgupta, CRISPR-based assays for rapid detection of SARS-CoV-2, Methods (2020).

[17] B.D. Kevadiya, J. Machhi, J. Herskovitz, M.D. Oleynikov, W.R. Blomberg, N. Bajwa, D. Soni, S. Das, M. Hasan, M. Patel, A.M. Senan, S. Gorantla, J. McMillan, B. Edagwa, R. Eisenberg, C.B. Gurumurthy, S.P.M. Reid, C. Punyadeera, L. Chang, H.E. Gendelman, Diagnostics for SARS-CoV-2 infections, Nat. Mater. 20 (5) (2021) 593–605.

[18] R. Chen, L. Kan, F. Duan, L. He, M. Wang, J. Cui, Zhi. Zhang, and Zho. Zhang, "Surface plasmon resonance aptasensor based on niobium carbide MXene quantum dots for nucleocapsid of SARS-CoV-2 detection," *Microchimica Acta*, vol. 188, no. 316, pp. 1-10, Sep. 2021.

[19] F. Narita, Z. Wang, H. Kurita, Z. Li, Y. Shi, Y. Jia, C. Soutis, A review of piezoelectric and magnetostrictive biosensor materials for detection of COVID-19 and other viruses, Adv. Mater. 33 (1) (Nov. 2020) 2005448.

[20] Y.-C. Peng, C.-H. Cheng, H. Yatsuda, S.-H. Liu, S.-J. Liu, T. Kogai, C.-Y. Kuo, R.Y. L. Wang, A novel rapid test to detect anti-SARS-CoV-2 N protein IgG based on shear horizontal surface acoustic wave (SH-SAW), Diagnostics 11 (10) (Oct. 2021) 1838.

[21] N. Kumar, N.P. Shetti, S. Jagannath, T.M. Aminabhavi, Electrochemical sensors for the detection of SARS-CoV-2 virus, Chem. Eng. J. 430 (3) (Feb. 2022) 132966.

[22] G.A. Naikoo, T. Awan, I.U. Hassan, H. Salim, F. Arshad, W. Ahmed, A.M. Asiri, A. Qurashi, Nanomaterials-based sensors for respiratory viral detection: a review, IEEE Sens. J. 21 (16) (Aug. 2021) 17643–17656.

[57] Tara Ghafouri, Negin Manavizadeh, Ebrahim Nadimi, Biosensing properties of zinc oxide nanoribbons toward creatine: A first-principles study, IEEE Sensors Journal (2022), https://doi.org/10.1109/JSEN.2022.3158700. In press.

[24] V. Ratautaite, R. Boguzaite, E. Brazys, A. Ramanaviciene, E. Ciplys, M. Juozapaitis, R. Slibinskas, M. Bechelany, A. Ramanavicius, Molecularly imprinted polypyrrole based sensor for the detection of SARS-CoV-2 spike glycoprotein, Electrochim. Acta 403 (Jan. 2022) 139581.

[25] H. Liu, A. Yang, J. Song, N. Wang, P. Lam, Y. Li, H.-W. Law, F. Yan, Ultrafast, sensitive, and portable detection of COVID-19 IgG using flexible organic electrochemical transistors, Sci. Adv. 7 (38) (2021).

[26] Q. Lin, D. Wen, J. Wu, L. Liu, W. Wu, X. Fang, J. Kong, Microfluidic immunoassays for sensitive and simultaneous detection of IgG/IgM/antigen of SARS-CoV-2 within 15 min, Anal. Chem. 92 (14) (Jul. 2020) 9454–9458.

[27] Q. Zhou, Y. Lin, K. Zhang, M. Li, D. Tang, Reduced graphene oxide/$BiFeO_3$ nanohybrids-based signal-on photoelectrochemical sensing system for prostate-specific antigen detection coupling with magnetic microfluidic device, Biosens. Bioelectron. 101 (2018) 146–152.

[28] Y. Lin, Q. Zhou, J. Li, J. Shu, Z. Qiu, Y. Lin, D. Tang, Magnetic graphene nanosheet-based microfluidic device for homogeneous real-time electronic monitoring of pyrophosphatase activity using enzymatic hydrolysate-induced release of copper ion, Anal. Chem. 88 (1) (Nov. 2015) 1030–1038.
[29] J.R. Mejía-Salazar, K.R. Cruz, E.M.M. Vásques, and O.N. de Oliveira Jr., "Microfluidic point-of-care devices: New trends and future prospects for ehealth diagnostics," *Sensors*, vol. 20, no. 7, p. 1951, Mar. 2020.
[30] C. Zhao, X. Liu, A portable paper-based microfluidic platform for multiplexed electrochemical detection of human immunodeficiency virus and hepatitis C virus antibodies in serum, Biomicrofluidics 10 (2) (Apr. 2016) 024119.
[31] H. Zhao, et al., Accessible detection of SARS-CoV-2 through molecular nanostructures and automated microfluidics, Biosens. Bioelectron. 194 (Dec. 2021) 113629.
[32] N. Soin, S.J. Fishlock, C. Kelsey, S. Smith, Triboelectric effect enabled self-powered, point-of-care diagnostics: opportunities for developing ASSURED and REASSURED devices, Micromachines 12 (3) (Mar. 2021) 337.
[33] Q. Zhou, J. Pan, S. Deng, F. Xia, T. Kim, Triboelectric nanogenerator-based sensor systems for chemical or biological detection, Adv. Mater. 33 (35) (Jul. 2021) 2008276.
[34] G. Khandelwal, N.P.M.J. Raj, S.-J. Kim, Triboelectric nanogenerator for healthcare and biomedical applications, Nano Today 33 (Aug. 2020) 100882.
[35] J. Li, S. Li, X. Qiu, W. Zhu, L. Li, B.o. Qin, Performance of diagnostic model for differentiating between COVID-19 and influenza: a 2-center retrospective study, Med. Sci. Monit. 27 (2021).
[36] M. Drobysh, A. Ramanaviciene, R. Viter, C.-F. Chen, U. Samukaite-Bubniene, V. Ratautaite, A. Ramanavicius, Biosensors for the determination of SARS-CoV-2 virus and diagnosis of COVID-19 infection, Int. J. Mol. Sci. 23 (2) (Jan. 2022) 666.
[58] Maryia Drobysh, Almira Ramanaviciene, Roman Viter, Arunas Ramanavicius, Affinity sensors for the diagnosis of COVID-19, Micromachines 12 (4) (2021) 390, https://doi.org/10.3390/mi12040390.
[37] Y. Huang, C. Yang, X.-F. Xu, W. Xu, S.-W. Liu, Structural and functional properties of SARS-CoV-2 spike protein: potential antivirus drug development for COVID-19, Acta Pharmacol. Sin. 41 (Aug. 2020) 1141–1149.
[38] P.H. Pawłowski, Charged amino acids may promote coronavirus SARS-CoV-2 fusion with the host cell, AIMS Biophys. 8 (1) (Jan. 2021) 111–120.
[39] F. Krebs, C. Scheller, K. Grove-Heike, L. Pohl, H. Wätzig, Isoelectric point determination by imaged CIEF of commercially available SARS-CoV-2 proteins and the hACE2 receptor, Electrophoresis 42 (6) (2021) 687–692.
[40] B. Michen, T. Graule, Isoelectric points of viruses, J. Appl. Microbiol. 109 (2) (2010) 388–397.
[41] H.-X. Zhou, X. Pang, Electrostatic interactions in protein structure, folding, binding, and condensation, Chem. Rev. 118 (4) (Feb. 2018) 1691–1741.
[42] I. Plikusiene, V. Maciulis, A. Ramanaviciene, Z. Balevicius, E. Buzavaite-Verteliene, E. Ciplys, R. Slibinskas, M. Simanavicius, A. Zvirbliene, A. Ramanavicius, Evaluation of kinetics and thermodynamics of interaction between immobilized SARS-CoV-2 nucleoprotein and specific antibodies by total internal reflection ellipsometry, J. Colloid Interface Sci. 594 (2021) 195–203.
[43] Z.S. Klestova, A.K. Voronina, A.Y. Yushchenko, O.S. Vatlitsova, G.V. Dorozinsky, Y. V. Ushenin, V.P. Maslov, T.P. Doroshenko, S.A. Kravchenko, Aspects of "antigen–antibody" interaction of chicken infectious bronchitis virus determined by surface plasmon resonance, Spectrochim. Acta A Mol. Biomol. Spectrosc. 264 (Jan. 2022) 120236.
[44] Q.-T. Nguyen, K.-K.-K. Ahn, Fluid-based triboelectric nanogenerators: A review of current status and applications, Int. J. Precis. Eng. Manuf.-Green Tech. 8 (Aug. 2020) 1043–1060.
[45] L. Pan, J. Wang, P. Wang, R. Gao, Y.-C. Wang, X. Zhang, J.-J. Zou, Z.L. Wang, Liquid-FEP-based U-tube triboelectric nanogenerator for harvesting water-wave energy, Nano Res. 11 (Feb. 2018) 4062–4073.
[46] Q. Zheng, G.-W. Wei, "Poisson–Boltzmann–Nernst–Planck model", J. Chem. Phys. 134 (19) (May 2011) 194101.
[47] L.L. Lu, T.J. Suscovich, S.M. Fortune, G. Alter, Beyond binding: antibody effector functions in infectious diseases, Nat. Rev. Immunol. 18 (1) (2018) 46–61.
[48] G. Trefalt, S.H. Behrens, M. Borkovec, Charge regulation in the electrical double layer: ion adsorption and surface interactions, Langmuir 32 (2) (2016) 380–400.
[49] T. Xue, W. Wu, N. Guo, C. Wu, J. Huang, L. Lai, H. Liu, Y. Li, T. Wang, and Y. Wang, "Single point mutations can potentially enhance infectivity of SARS-CoV-2 revealed by in silico affinity maturation and SPR assay," *RSC Adv.*, vol. 11, pp. 14737-14745, May. 2021.
[50] S.C.B. Gopinath, P.K.R. Kumar, Aptamers that bind to the hemagglutinin of the recent pandemic influenza virus H1N1 and efficiently inhibit agglutination, Acta Biomater. 9 (11) (Nov. 2013) 8932–8941.
[51] W. Kim, D. Choi, J.-Y. Kwon, D. Choi, Self-powered triboelectric microfluidic system for liquid sensing, J. Mater. Chem. A 6 (Jun. 2018) 14069–14076.
[52] M.A. Ahmad, F. Mustafa, L.M. Ali, J.V. Karakkat, T.A. Rizvi, Label-free capacitance-based identification of viruses, Sci. Rep. 5 (1) (May 2015).
[53] S. Niu, Y. Liu, S. Wang, L. Lin, Y.S. Zhou, Y. Hu, Z.L. Wang, Theoretical investigation and structural optimization of single-electrode triboelectric nanogenerators, Adv. Funct. Mater. 24 (22) (Feb. 2014) 3332–3340.
[54] J. Shang, G. Ye, K.e. Shi, Y. Wan, C. Luo, H. Aihara, Q. Geng, A. Auerbach, F. Li, Structural basis of receptor recognition by SARS-CoV-2, Nature 581 (7807) (2020) 221–224.
[55] E. van der Vries, P.J. Collins, S.G. Vachieri, X. Xiong, J. Liu, P.A. Walker, L.F. Haire, A.J. Hay, M. Schutten, A.D.M.E. Osterhaus, S.R. Martin, C.A.B. Boucher, J. J. Skehel, S.J. Gamblin, F.A. Rey, H1N1 2009 pandemic influenza virus: resistance of the I223R neuraminidase mutant explained by kinetic and structural analysis, PLoS Pathog. 8 (9) (Sep. 2012) e1002914.
[56] C. Wang, P. Wang, J. Chen, L. Zhu, D. Zhang, Y. Wan, S. Ai, Self-powered biosensing system driven by triboelectric nanogenerator for specific detection of Gram-positive bacteria, Nano Energy 93 (Mar. 2022) 106828.